

Unsupervised GAN-CIRCLE for High-Resolution Reconstruction of Bone Microstructure from Low-Resolution CT Scans

Indranil Guha,^{a,*} Syed Ahmed Nadeem,^a Xiaoliu Zhang,^a Steven M Levy,^c James C Torner,^d Punam K Saha^{a,b}

^aDepartment of Electrical and Computer Engineering, College of Engineering, University of Iowa, Iowa City, IA 52242

^bDepartment of Radiology, Carver College of Medicine, University of Iowa, Iowa City, IA 52242

^cDepartment of Preventive and Community Dentistry, College of Dentistry, University of Iowa, Iowa City, IA 52242

^dDepartment of Epidemiology, University of Iowa, Iowa City, IA 52242

ABSTRACT

Osteoporosis is an age-related disease associated with reduced bone density and increased fracture-risk. It is known that bone microstructural quality is a significant determinant of trabecular bone strength and fracture-risk. Emerging CT technology allows high-resolution *in vivo* imaging at peripheral sites enabling assessment of bone microstructure at low radiation. Resolution dependence of bone microstructural measures together with varying technologies and rapid upgrades in CT scanners warrants data-harmonization in multi-site as well as longitudinal studies. This paper presents an unsupervised deep learning method for high-resolution reconstruction of bone microstructure from low-resolution CT scans using GAN-CIRCLE. The unsupervised training alleviates the need of registered low- and high-resolution images, which is often unavailable. Low- and high-resolution ankle CT scans of twenty volunteers were used for training, validation, and evaluation. Ten thousand unregistered low- and high-resolution patches of size 64×64 were randomly harvested from CT scans of ten volunteers for training and validation. Five thousand matched pairs of low- and high-resolution patches were generated for evaluation after registering CT scan pairs from other ten volunteers. Quantitative comparison shows that predicted high-resolution scans have significantly improved structural similarity index ($p < 0.01$) with true high-resolution scans as compared to the same metric derived from low-resolution data. Also, trabecular bone microstructural measures such as thickness and network area measures computed from predicted high-resolution CT images showed higher (CCC = [0.90, 0.84]) agreement with the reference measures from true high-resolution scans compared to the same measures derived from low-resolution images (CCC = [0.66, 0.83]).

Keywords: GAN-CIRCLE, high-resolution reconstruction, deep learning, osteoporosis, trabecular bone, microstructure.

1. INTRODUCTION

Osteoporosis is a bone disease characterized by reduced bone mineral density (BMD), degenerated bone microstructure and enhanced fracture-risk. Although osteoporosis is a disease across all ages and both genders, its prevalence grows with aging, especially among Caucasians and women after menopause.¹ Approximately, 40% of women and 13% of men suffer osteoporotic fractures in their lifetime, and increased life expectancy will increase fracture incidence to 6.3 million by 2050.² Dual-energy X-ray absorptiometry (DXA) measured areal BMD is the clinical standard for diagnosis of osteoporosis. It has been shown that BMD explains 60-70% of the variability in bone strength and fracture-risk,³ and the remaining variability comes from the collective effect of other factors such as cortical and trabecular bone distribution, and their microstructural basis.⁴⁻⁶ Thus, standardized imaging methods for quantitative and effective assessment of bone microstructure is an urgent need for research and clinical bone studies.

*indranil-guha@uiowa.edu

Various topologic and geometric methods are available in literature to measure trabecular bone (Tb) micro-structure.⁷⁻¹⁰ Vesterby *et al.*⁷ conceived a stereological parameter, called star volume, which is the average volume of an object region that can be seen from a point inside that region unobscured in all directions. Hahn *et al.*⁸ introduced the “trabecular bone pattern factor” which captures Tb connectivity in terms of the convexity property of the Tb surface defined as the ratio of the differences in perimeter and area under dilation. Hildebrand *et al.*⁹ developed a three-dimensional (3-D) structure model index, a function of global plate-to-rod ratio, based on the observation that the rate of volume change with respect to half thickness (or the radius) for plate-like elements is different from that for rod-like elements. Feldkamp *et al.*¹⁰ showed that the makeup of Tb networks can be expressed in terms of topological entities such as the 3-D Euler number. Saha and his colleagues have pioneered unique algorithms,¹¹⁻¹⁸ characterizing individual trabecular plates and rods, which have been adopted in a large number of studies.^{12-15,19-38}

Several 3-D bone micro-imaging modalities, including magnetic resonance imaging (MRI)^{3,39-41} and high-resolution peripheral quantitative computed tomography (HR-pQCT),⁴²⁻⁴⁴ have been popularly applied in bone studies. Emerging multi-detector-row CT (MDCT) scanners allow high-speed and high-resolution *in vivo* imaging at peripheral sites enabling segmentation and assessment of bone microstructure at low radiation. MDCT technologies overcome the major deficits of MRI and HR-pQCT modalities related to slow scan speed, limited field-of-view and failure to provide quantitative BMD for MRI.^{42,45} However, lack of standardization of MDCT based bone microstructural measures is a major concern in multi-site as well as longitudinal bone studies, which emerges from wide discrepancies in spatial resolution, and other imaging and reconstruction features from different vendors and rapid upgrades in technology. Often, in longitudinal studies old scanner gets substituted by a new and upgraded scanner at the middle of the study causing inconsistency in data acquisition and analysis or even a waste of previous data collected using the older machine. It initiates the need of data harmonization, which will enable researchers to plan study design involving data collection from different scanners improving the fidelity of multi-site or longitudinal studies. Although high-resolution (HR) imaging of Tb can be achieved by using sophisticated hardware components such as high pitch detector, x-ray tube with fine focal spot etc. it reduces scan speed and increases CT-machine cost as well as radiation dose. Hence, computational methods have gained popularity for reconstruction of HR images from their low-resolution (LR) counterpart and such methods can be divided into two broad categories: (1) model-based reconstruction techniques, and (2) learning-based methods.

Model-based reconstruction algorithms uses prior assumption about the image degradation process to regulate the reconstruction of HR image features.⁴⁶⁻⁴⁸ In contrast learning-based methods learns a non-linear mapping function to reconstruct HR image from the LR counterpart.⁴⁹⁻⁵² Numerous deep learning (DL) based methods have shown promising results in HR reconstruction for different *in vivo* CT modalities.⁵²⁻⁵⁷ Chen *et al.*⁵⁸ developed a deep densely connected network for super resolution (SR) reconstruction of MR images. Chaudhury *et al.*⁵⁴ trained a 3-D convolutional neural network (CNN) for SR reconstruction of MR images using paired high- and low-resolution image slices. Park *et al.*⁵⁵ proposed an U-net based SR reconstruction technique for CT images. Yu *et al.*⁵⁶ combined a single-slice CT SR network (s-CTSRN) with skip connections and a multi-slice CT SR network (m-CTSRN) to reconstruct SR CT images. Generative adversarial network (GAN) has been widely used for SR reconstruction of Tb microstructure. One of the reasons for vast popularity of GAN based methods for SR reconstruction is that they can be trained in unsupervised fashion which does not require matching pairs of LR and HR datasets.^{57,59-62} Ledig *et al.* trained a GAN based SR reconstruction method (SRGAN) where the objective function is defined as a weighted sum of adversarial and content loss functions.⁵⁹ Wang *et al.* used Residual-in-Residual Dense Block (RRDB) without batch normalization as the building block of SRGAN to eliminate noisy artifacts in reconstructed SR images using SRGAN.⁶⁰ Wolterink *et al.* trained an unsupervised GAN to learn the non-linear mapping from LR to HR images and successfully enhanced the image quality.⁶¹ You *et al.* developed a two-dimensional (2-D) CT based SR reconstruction technique using GAN constrained by the identical, residual, and cycle consistency loss (GAN-CIRCLE).⁵⁷

In this paper, we present an unsupervised DL based method for HR reconstruction of bone microstructure from LR CT scans using GAN-CIRCLE and evaluate its performance in terms of image quality as well as different microstructural measures.^{57,62} The facility of unsupervised learning alleviates the need for registering low- and high-resolution CT images, which is often unavailable. DL network architecture, data acquisition protocols, post-processing steps, computation of microstructural measures, and statistical methods used for evaluation are elaborated in section 2. Experimental results are described in Section 3, and the conclusions are drawn in Section 4.

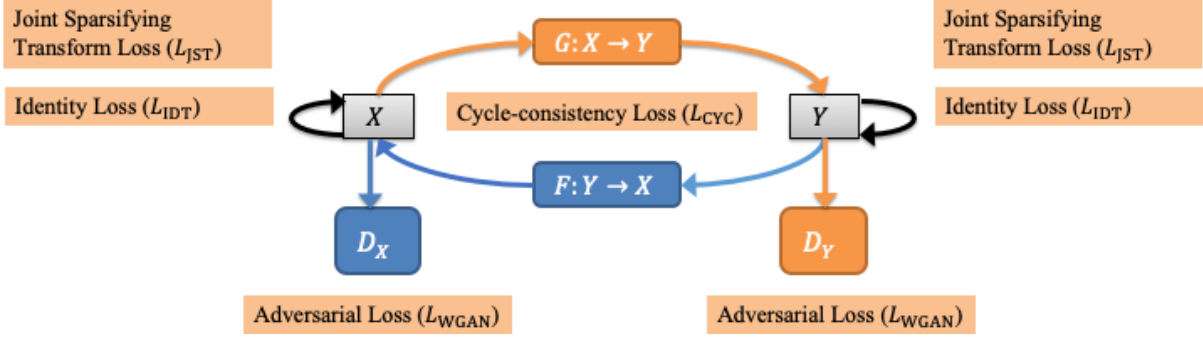


Figure 1. Basic principle of GAN-CIRCLE for HR CT image reconstruction. Here, X is the set of LR CT scans, and Y is the set of HR scans. The network comprises of two basic GAN modules (G, D_Y) and (F, D_X), each consisting of a generator and a discriminator; and these modules are responsible for low-high and high-low resolution image reconstruction, respectively. Different loss functions are synergistically reduced by the network, while regularization terms related to cycle-consistency and identity loss prevents the network from overfitting.

2. METHODOLOGY

In this section, we describe (1) the network architecture of GAN-CIRCLE, CT scan protocols on low- and high-resolution MDCT scanners, (2) steps for harvesting LR and HR patches for training, validation, and testing, (3) different Tb microstructural measures examined in this paper, and (4) the statistical metrics used for evaluating these measures.

2.1 Deep Learning Network Architecture

A new deep learning network is developed using the basic principle of GAN-CIRCLE (Figure 1) and trained in an unsupervised manner, i.e. using unpaired LR and HR two dimensional (2-D) patches, to successfully recover HR bone microstructural features from a LR CT scan through non-linear deblurring and filtering. GAN-CIRCLE consists of two generator mappings $G: X \rightarrow Y$ and $F: Y \rightarrow X$, where X is the set of LR CT scans and Y is the set of HR CT scans. The overall goal of this network is to optimize the low-to-high resolution generator ($G: X \rightarrow Y$) to learn the nonlinear mapping from low- to high-resolution CT scans while synergistically minimizing the cycle-consistency, adversarial, identity and joint sparsifying transform loss functions. The quality of the generator G is directly controlled using a discriminator D_Y and the associated adversarial loss function L_{WGAN} . During the learning process, both generator G and discriminator D_Y compete against each other, thus synergistically improving themselves while reducing the adversarial loss. To prevent the network from overfitting, a cycle-consistency check is added through a counter generator $F: Y \rightarrow X$ from HR to LR, and a cycle-consistency loss function L_{CYC} . Similar to the generator G , the learning process of F is controlled using another discriminator D_X associated with adversarial loss function L_{WGAN} . The training process is regularized by an identity loss function L_{IDT} to prevent the network from generating a significantly different output when a true HR (or LR) patch is fed as an input to the generator G (or F). Finally, a joint sparsifying transformation loss function L_{JST} is used for simultaneously sparsifying predicted images and reducing noise, while preserving anatomical features by minimizing the difference from the true HR image. So, during training the network tries to minimize the following objective function:

$$L_{GAN-CIRCLE} = L_{WGAN}(D_Y, G) + L_{WGAN}(D_X, F) + \lambda_1 L_{CYC}(G, F) + \lambda_2 L_{IDT}(G, F) + \lambda_3 L_{JST}(G),$$

where, λ_1, λ_2 , and λ_3 are the weights for different losses.⁵⁷

Network architectures of the generators (G and F), and the discriminators (D_X and D_Y) are shown in Figure 2 and Figure 3 respectively. Generator network consists of a feature extraction module and a reconstruction module. Feature extraction module is a concatenation of 12 non-linear SR blocks where each block consists of 3×3 convolution kernels, bias, leaky rectified linear unit (Leaky ReLU), and a dropout layer. Same number of filters as suggested by You *et al.*⁵⁷ are used in each block. At all convolution layers stride is set to 1 except for the first layer where stride is 2. Finally, outputs of the SR blocks are concatenated using a skip connection before feeding into the reconstruction module to prevent overfitting and training saturation.

A network in network architecture is adopted for the reconstruction module which consists of two parallel branches of CNNs and output from these two branches are concatenated before up sampling by a factor of 2. Two SR blocks, with 1×1 convolution kernel, are used in the two parallel branches to reduce dimensionality while increasing non-linearity of the

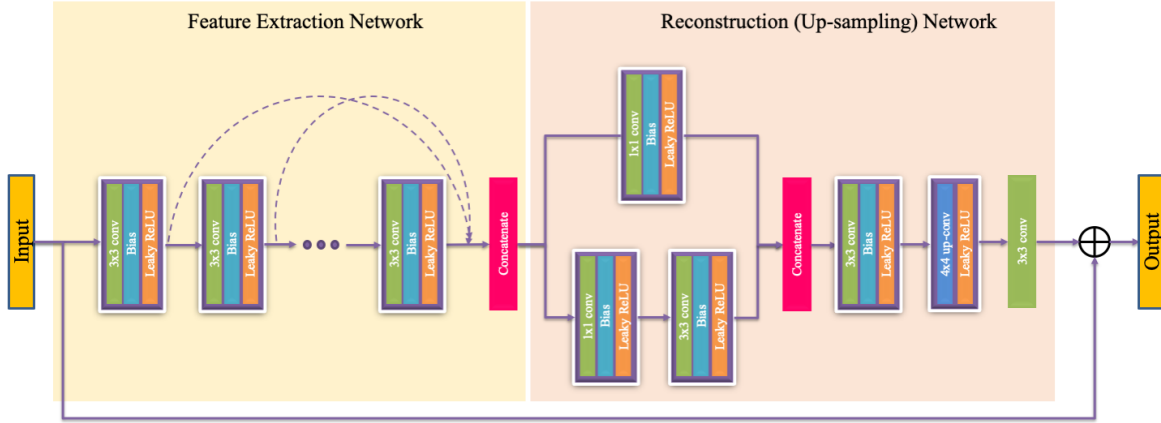


Figure 2. Architecture of a generator. Stride within each convolution layer is 1 except for the first layer where the stride is 2.

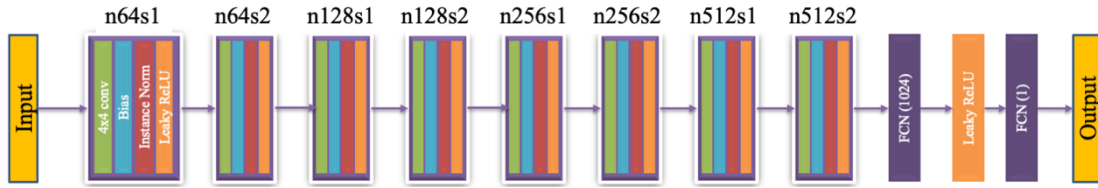


Figure 3. Architecture of a discriminator. Here, n denotes the number of kernels in a convolutional layer, and s denotes the stride.

network. In the last convolutional block of the reconstruction network all the feature maps are fused to generate a residual image with all the high frequency details of the LR image. Finally, the input image is combined with the residual image to obtain the predicted HR image.

The discriminator network is composed of 8 convolution layers with 64, 64, 128, 128, 256, 256, 512, and 512 filters respectively followed by two fully connected (FCN) layers with 1024 outputs and 1 output.

2.2 Dataset Description

The GAN-CIRCLE based HR reconstructor of bone microstructure was trained, validated and tested using LR and HR CT scans of human volunteers. Specifically, the distal tibia from left legs of twenty healthy volunteers (age: 26.2 ± 4.5 Y; 10 F) were scanned on two MDCT scanners. The study was conducted around the transition period of the MDCT scanner upgrade at the University of Iowa Comprehensive Lung Imaging Center (ICLIC). Distal tibia of each volunteer was first scanned on a LR Siemens FLASH scanner, and then they were recalled and rescanned on a HR Siemens FORCE scanner after upgrade. The average time gap between the LR and HR scans were 44.6 ± 2.7 days with the minimum and maximum gaps of 40 and 48 days, respectively. The human study was approved by The University of Iowa Institutional Review Board and all participants provided written informed consent. The CT scan protocols on the two scanners are described in the following.

FLASH scanner: Single X-ray source spiral acquisition at 120 kV, 200 effective mAs, 1 sec rotation speed, pitch factor: 1.0, total effective dose equivalent: $170 \mu\text{Sv} \approx 20$ days of environmental radiation in the U.S. Images were reconstructed at $200 \mu\text{m}$ slice-spacing using a normal cone beam method with a special U70u kernel.

FORCE scanner: Single X-ray source spiral acquisition at 120 kV, 100 effective mAs, 1 sec rotation speed, pitch factor: 1.0, total effective dose equivalent: $50 \mu\text{Sv} \approx 5$ days of environmental radiation in the U.S. Images were reconstructed at $200 \mu\text{m}$ slice-spacing and $150 \mu\text{m}$ pixel-size using Siemens's special kernel Ur77u with Edge Technology.

For both scanners, Siemens z-UHR scan mode was applied, enabling Siemens double z sampling technology and achieving high structural resolution.

2.3 Data Processing, Training, and Validation

A Gammex RMI 467 Tissue Characterization Phantom (Gammex RMI, Middleton, WI) was used to calibrate both LR and HR CT Hounsfield numbers into BMD values. After calibration LR images were interpolated at $150 \mu\text{m}$ isotropic voxel

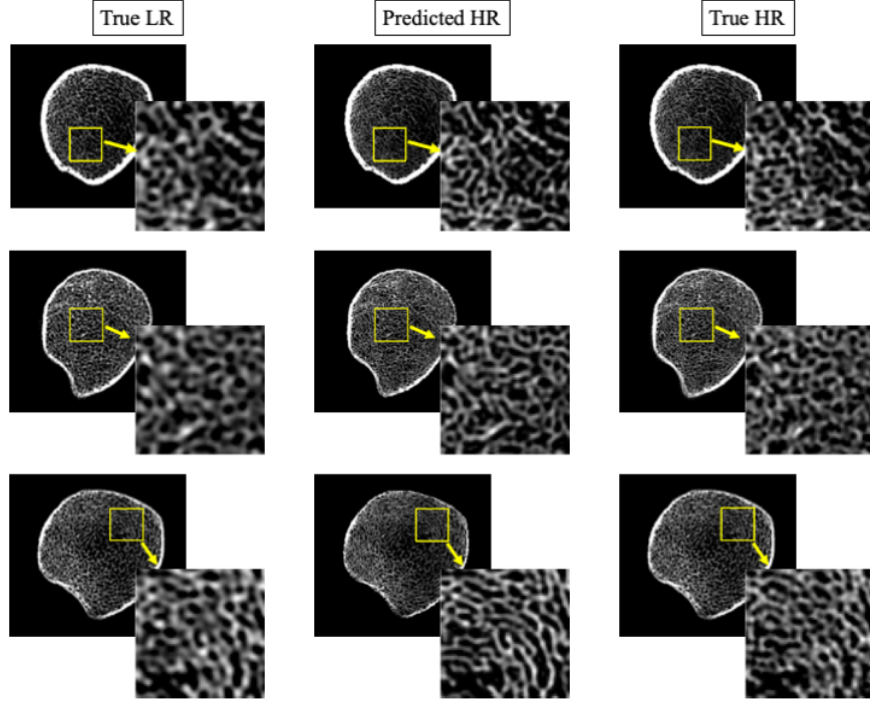


Figure 4. Reconstructed HR images from LR CT scans using GAN-CIRCLE and comparison with true HR scan data. Each row presents matching original and reconstructed axial image slices from a human distal tibia dataset. Left-to-right columns: a 2-D image slice from a LR CT scan on a Siemens FLASH scanner (left); predicted HR image slice from the LR CT data (middle); and true HR image slice from post-registered Siemens FORCE scan (right).

size using windowed sinc interpolation.⁶³ Ten out of twenty pairs of LR and HR BMD images were used for training and validation of the HR reconstructor. The other ten pairs of LR and HR images were used for testing after registering HR images to corresponding LR images. Registration of HR images to the corresponding LR scans were performed in two steps— first, cortical bone and Tb network of the HR image was manually registered to the LR image using ITK-SNAP registration toolkit.⁶⁴ In the second step, a rigid transformation was applied on the manually registered HR image for fine tuning, where registration process was initialized using the transformation matrix from the manual registration step. To improve the registration accuracy, region of interest (ROI) for registration cost function was defined as the distal tibia with a soft boundary. Ten thousand LR and ten thousand HR patches of size 64×64 were independently harvested from LR and HR BMD images of ten volunteers for training. A different set of five thousand pairs of matching LR and HR patches from registered BMD images of ten other volunteers were used for testing and evaluation. Low- and high-resolution patches were randomly harvested from 30% peeled ROIs of LR and HR BMD images, and normalized to the unit interval of $[0, 1]$.

Table 1. List of CT-derived trabecular bone measures examined in this paper. Nomenclatures of trabecular bone measures used by Bouxsein *et al.*⁶⁷ and Chen *et al.*⁵³ are followed here wherever possible.

Parameter (unit)	Description
Tb.NA (mm^2/mm^3)	Tb network area density, i.e., the average area of the medial surface of segmented bone per unit ROI
Tb.Th (μm)	Mean trabecular thickness computed by star-line analysis ⁶⁸
Tb.Sp (μm)	Mean trabecular spacing, i.e., the space between trabecular microstructures computed by star-line analysis ⁶⁸

For training, weights of the convolution layers were initialized using the techniques proposed by He *et al.*⁶⁵ During the training weights λ_1, λ_2 , and λ_3 were set to 1, 0.5, and 0.001 respectively. Slope of the leaky ReLU was set to 0.1 and drop out was applied to each convolution layer with $p = 0.8$. The network was trained for 2000 epochs and took almost two days to train using Adam optimizer⁶⁶ with $\beta_1 = 0.5$ and $\beta_2 = 0.9$ and a learning rate of 1×10^{-4} .

2.4 Computation of Tb Microstructural Measures

Tb measures used to evaluate the DL network are listed in Table 1. Following image processing steps were applied to each BMD image – (1) fuzzy skeletonization⁶⁹ and computation of trabecular network area density (Tb.NA) measure and (2) star-line analysis for computation of trabecular thickness (Tb.Th) and trabecular spacing (Tb.Sp) measures.⁶⁸ Note that all Tb measures were computed on 2-D slices of LR, true HR and predicted HR images.

2.5 Statistical Analysis

The performance of the network was quantitatively evaluated using structural similarity (SSIM) index⁷⁰— a widely used method to estimate perceived quality of images and videos. SSIM was computed between LR and true HR, as well as between predicted HR and true HR patches. Tb thickness, spacing, and network area measurements on 2-D slices were stacked to reconstruct a 3-D representation of the measures, and mean and standard deviation (SD) of each Tb measure from LR, true HR and predicted HR scans were computed over 100 randomly selected spherical ROIs of 12-pixel radius. All spherical ROIs were fully confined within the 30% peeled ROI of each scan. Finally, for each specimen linear correlation (r-value) and concordance correlation coefficients (CCC) were computed between the mean values of Tb measures derived from true HR and LR images as well as true and predicted HR images.

3. EXPERIMENTS AND RESULTS

Results of HR image reconstruction from LR images using GAN-CIRCLE are illustrated in Figure 4. Predicted HR images (middle row) from three LR images (left row) as well as matching true HR images (right column) are shown for visual comparison in Figure 4. HR reconstruction of a full image slice was obtained by independently reconstructing non-overlapping 64×64 patches and stitching them together. It is worth mentioning that despite independent patch reconstruction no block effects are visible in the predicted HR images which suggests that cycle-consistency and other regularization constraints of the GAN-CIRCLE can avoid random patch-bias artifacts. For each example a matching 64×64 patch from the LR, true and predicted HR slices is zoomed in to display the performance of the method at the level of Tb microstructures. Visual comparison of the matching zoomed in patches shows that the GAN-CIRCLE successfully performs a non-linear deblurring and filtering to reconstruct HR Tb microstructural features from blurred and noisy LR data.

Table 2. Mean and standard deviation (mean \pm SD) of linear and concordance correlation coefficients of LR and predicted HR derived Tb measures w.r.t the reference measures from true HR images for individual subjects.

Tb Measures	LR vs. True HR		Predicted HR vs. True HR	
	Linear Correlation (r)	CCC	Linear Correlation (r)	CCC
Tb.Th (μm)	0.95 ± 0.02	0.66 ± 0.12	0.96 ± 0.02	0.90 ± 0.06
Tb.Sp (μm)	0.96 ± 0.02	0.93 ± 0.05	0.96 ± 0.04	0.94 ± 0.05
Tb.NA (mm^2/mm^3)	0.88 ± 0.07	0.83 ± 0.11	0.88 ± 0.05	0.84 ± 0.12

For quantitative evaluation four thousand patches entirely lying inside the Tb region were used. SSIM values was computed between LR and true HR, as well as between predicted HR and true HR patches and the results of the paired t-test suggest that the reconstruction network significantly improves ($p < 0.01$) the structural similarity with the true HR images. Mean and standard deviation of the r-values and CCCs of Tb.Th, Tb.Sp, and Tb.NA measures from ten test subjects are presented in Table 2. No significant difference ($p > 0.05$) was observed between the r-values from LR and true HR images, as well as the predicted and true HR images for all three Tb measures. Agreement between the Tb measures computed from predicted HR and LR images and the reference measures derived from the true HR scan was evaluated in terms of CCC. CCC observed between Tb measures derived from predicted and true HR images was higher than the CCC measured between Tb measures from LR and true HR images. Most significant improvement in CCC was observed for Tb.Th ($p <$

0.0001) measure, where mean CCC increased from 0.66 for LR and true HR images to 0.95 for predicted and true HR images. However, relatively smaller improvement in CCC was noticed for Tb.Sp ($p < 0.01$) and Tb.NA ($p < 0.01$) measure as compared to Tb.Th.

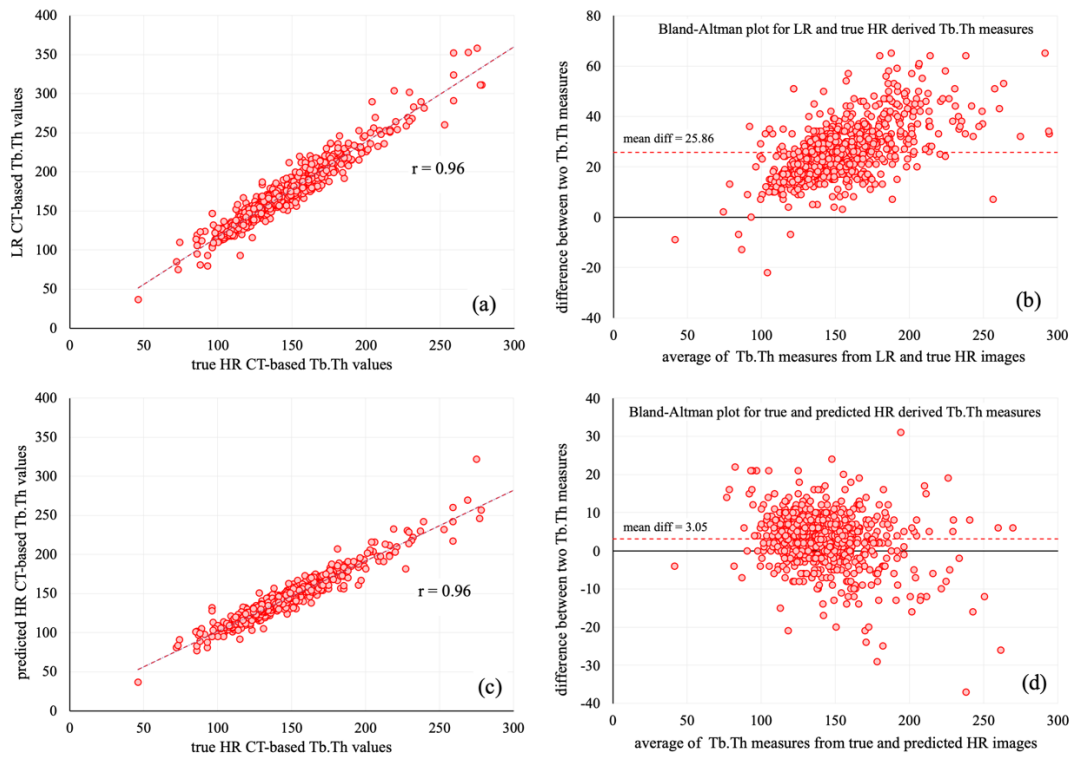


Figure 5. Linear correlation and Bland-Altman plots of Tb.Th measures computed from LR, HR, and predicted HR images of ten test subjects. (a,b) Linear correlation analysis (a) and Bland-Altman plot (b) of Tb.Th values derived from LR and true HR images. (c,d) Same as (a,b) but for Tb.Th measured derived from true and predicted HR images.

CCC and r-values from the combined analysis of Tb measurements from ten test subjects are reported in Table 3. No significant change was observed for r-values of Tb measures computed from LR and predicted HR images, and true and predicted HR images. For the combined analysis CCC between Tb.Th values from LR and true HR images was found

Table 3. Results of combined linear and concordance correlation analysis of different Tb measures derived from LR, HR, and predicted HR images of test test subjects.

Tb Measures	LR – True HR		Predicted HR – True HR	
	Linear Correlation (r)	CCC	Linear Correlation (r)	CCC
Tb.Th (μm)	0.95	0.72	0.96	0.90
Tb.Sp (μm)	0.94	0.90	0.97	0.92
Tb.NA (mm^2/mm^3)	0.87	0.82	0.90	0.83

to be 0.72 while for predicted and true HR CCC was 0.90. Linear correlation (a,c) and Bland-Altman plot (b,d) of Tb.Th measurements from ten test subjects are shown in Figure 5. As can be seen from (b) and (d), mean difference between Tb.Th measurements from true and predicted HR images are significantly lower than the mean difference in Tb.Th values from LR and true HR images. This observation suggests that the proposed HR reconstructor successfully reduces the bias in Tb.Th measures from LR images. However, when combined no significant improvement in CCC was noticed for Tb.Sp

and Tb.NA. CCC of Tb.Sp and Tb.NA measures derived from LR and true HR images were 0.90 and 0.82 respectively, whereas CCC for both measures derived from predicted and true HR images were 0.92 and 0.83 respectively.

4. CONCLUSIONS

In this paper, we have developed and evaluated an unsupervised deep learning-based method for HR reconstruction of bone microstructure from LR CT scans using GAN-CIRCLE. The unsupervised training method eliminates the need for registered pairs of low and high-resolution images, which is often not available or even not feasible. The network has been evaluated qualitatively as well as quantitatively on human ankle CT scans from two different scanners with different image-resolution features. Results of quantitative evaluative experiments have shown that the HR reconstructor not only improves the quality of LR images but also improves the agreement of Tb microstructural measures with the same measures derived from true HR images. These observations suggest that the new HR reconstructor will further improve the fidelity of both cross-sectional and longitudinal studies by allowing data harmonization to overcome challenges related to discrepancies in imaging facilities and features at different research performance sites.

ACKNOWLEDGEMENTS

This work was supported in part by the NIH grant R01 HL142042.

REFERENCES

- [1] The World Health Organization Bulletin, "Aging and Osteoporosis," 1999.
- [2] C Cooper, G Campion, and LJ Melton, 3rd, "Hip fractures in the elderly: a world-wide projection," *Osteoporosis International*, **2**, 285-289, 1992.
- [3] FW Wehrli, PK Saha, BR Gomberg, HK Song, PJ Snyder, M Benito, A Wright, and R Weening, "Role of magnetic resonance for assessing structure and function of trabecular bone," *Topics in Magnetic Resonance Imaging* **13**, 335-355, 2002.
- [4] M Kleerekoper, AR Villanueva, J Stanciu, DS Rao, and AM Parfitt, "The role of three-dimensional trabecular microstructure in the pathogenesis of vertebral compression fractures," *Calcified Tissue International* **37**, 594-597, 1985.
- [5] AM Parfitt, CHE Mathews, AR Villanueva, M Kleerekoper, B Frame, and DS Rao, "Relationships between surface, volume, and thickness of iliac trabecular bone in aging and in osteoporosis - implications for the microanatomic and cellular mechanisms of bone loss," *Journal of Clinical Investigation*, **72**, 1396-1409, 1983.
- [6] E Legrand, D Chappard, C Pascaretti, M Duquenne, S Krebs, V Rohmer, MF Basle, and M Audran, "Trabecular bone microarchitecture, bone mineral density, and vertebral fractures in male osteoporosis," *Journal of Bone and Mineral Research*, **15**, 13-19, 2000.
- [7] A Vesterby, HJ Gundersen, and F Melsen, "Star volume of marrow space and trabeculae of the first lumbar vertebra: sampling efficiency and biological variation," *Bone*, **10**, 7-13, 1989.
- [8] M Hahn, M Vogel, M Pompesius-Kempa, and G Delling, "Trabecular bone pattern factor--a new parameter for simple quantification of bone microarchitecture," *Bone*, **13**, 327-30, 1992.
- [9] T Hildebrand and P Rüegsegger, "Quantification of bone microarchitecture with the structure model index," *Computer Methods in Biomechanics and Biomedical Engineering*, **1**, 15-23, 1997.
- [10] LA Feldkamp, SA Goldstein, AM Parfitt, G Jesion, and M Kleerekoper, "The direct examination of three-dimensional bone architecture in vitro by computed tomography," *Journal of Bone and Mineral Research*, **4**, 3-11, 1989.
- [11] PK Saha and BB Chaudhuri, "Detection of 3-D simple points for topology preserving transformations with application to thinning," *IEEE Transactions on Pattern Analysis and Machine Intelligence*, **16**, 1028-1032, 1994.
- [12] PK Saha and BB Chaudhuri, "3D digital topology under binary transformation with applications," *Computer Vision and Image Understanding*, **63**, 418-429, 1996.
- [13] PK Saha, BB Chaudhuri, and DD Majumder, "A new shape preserving parallel thinning algorithm for 3D digital images," *Pattern Recognition*, **30**, 1939-1955, 1997.
- [14] PK Saha, BR Gomberg, and FW Wehrli, "Three-dimensional digital topological characterization of cancellous bone architecture," *International Journal of Imaging Systems and Technology*, **11**, 81-90, 2000.

- [15] BR Gomberg, PK Saha, HK Song, SN Hwang, and FW Wehrli, "Topological analysis of trabecular bone MR images," *IEEE Transactions on Medical Imaging*, **19**, 166-174, 2000.
- [16] XS Liu, P Sajda, PK Saha, FW Wehrli, G Bevill, TM Keaveny, and XE Guo, "Complete volumetric decomposition of individual trabecular plates and rods and its morphological correlations with anisotropic elastic moduli in human trabecular bone," *J Bone Miner Res*, **23**, 223-35, 2008, PubMed Central PMCID: PMC2665696.
- [17] PK Saha, Y Xu, H Duan, A Heiner, and G Liang, "Volumetric topological analysis: a novel approach for trabecular bone classification on the continuum between plates and rods," *IEEE transactions on medical imaging*, **29**, 1821-1838, 2010.
- [18] PK Saha, Y Liu, C Chen, D Jin, EM Letuchy, Z Xu, RE Amelon, TL Burns, JC Torner, SM Levy, and CA Calarge, "Characterization of trabecular bone plate-rod microarchitecture using multirow detector CT and the tensor scale: Algorithms, validation, and applications to pilot human studies," *Medical Physics*, **42**, 5410-5425, 2015, PubMed Central PMCID: PMC4545095.
- [19] G Chang, SK Pakin, ME Schweitzer, PK Saha, and RR Regatte, "Adaptations in trabecular bone microarchitecture in Olympic athletes determined by 7T MRI," *Journal of Magnetic Resonance in Medicine*, **27**, 1089-1095, 2008, PubMed Central PMCID: PMC3850284.
- [20] XS Liu, P Sajda, PK Saha, FW Wehrli, G Bevill, TM Keaveny, and XE Guo, "Complete volumetric decomposition of individual trabecular plates and rods and its morphological correlations with anisotropic elastic moduli in human trabecular bone," *Journal of Bone and Mineral Research*, **23**, 223-235, 2008.
- [21] PK Saha, Y Liu, C Chen, D Jin, EM Letuchy, Z Xu, RE Amelon, TL Burns, JC Torner, and SM Levy, "Characterization of trabecular bone plate-rod microarchitecture using multirow detector CT and the tensor scale: Algorithms, validation, and applications to pilot human studies," *Medical Physics*, **42**, 5410-5425, 2015.
- [22] M Stauber and R Muller, "Volumetric spatial decomposition of trabecular bone into rods and plates--a new method for local bone morphometry," *Bone*, **38**, 475-84, 2006.
- [23] G Chang, L Wang, G Liang, JS Babb, PK Saha, and RR Regatte, "Reproducibility of subregional trabecular bone micro-architectural measures derived from 7-Tesla magnetic resonance images," *MAGMA*, **24**, 121-5, 2011, PubMed Central PMCID: PMC3710719.
- [24] G Chang, L Wang, G Liang, JS Babb, GC Wiggins, PK Saha, and RR Regatte, "Quantitative assessment of trabecular bone micro-architecture of the wrist via 7 Tesla MRI: preliminary results," *MAGMA*, **24**, 191-9, 2011, PubMed Central PMCID: PMC3723135.
- [25] S Dudley-Javoroski, PK Saha, G Liang, C Li, Z Gao, and RK Shields, "High dose compressive loads attenuate bone mineral loss in humans with spinal cord injury," *Osteoporosis International*, **23**, 2335-2346, 2012, PubMed Central PMCID: PMC3374128.
- [26] S Dudley-Javoroski, R Amelon, YX Liu, PK Saha, and RK Shields, "High bone density masks architectural deficiencies in an individual with spinal cord injury," *Journal of Spinal Cord Medicine*, **37**, 349-354, 2014, PubMed Central PMCID: PMC4064585.
- [27] GA Ladinsky, B Vasilic, AM Popescu, M Wald, BS Zemel, PJ Snyder, L Loh, HK Song, PK Saha, AC Wright, and FW Wehrli, "Trabecular structure quantified with the MRI-based virtual bone biopsy in postmenopausal women contributes to vertebral deformity burden independent of areal vertebral BMD," *J Bone Miner Res*, **23**, 64-74, 2008, PubMed Central PMCID: PMC2663589.
- [28] M Benito, B Gomberg, FW Wehrli, RH Weening, B Zemel, AC Wright, HK Song, A Cucchiara, and PJ Snyder, "Deterioration of trabecular architecture in hypogonadal men," *The Journal of Clinical Endocrinology and Metabolism*, **88**, 1497-502, 2003.
- [29] PK Saha, Y Liu, TL Burn, JC Torner, and SM Levy, "Effects of physical activity on trabecular bone micro-architecture: a comparative study in young men and women using multi-detector CT and volumetric topological analysis," Proc. of *IEEE International Conference on Intelligent Computation and Bio-Medical Instrumentation*, 283-286, Wuhan, China, December 14-17 2011.
- [30] PK Saha, Y Liu, P C. A, TL Burns, JC Torner, and SM Levy, "Quantitative bone micro-architecture in young adults using multi-detector CT imaging and volumetric topological analysis – a feasibility study," Proc. of *Annual Meeting of the American Society for Bone and Mineral Research*, San Diego, CA, 2011.
- [31] PK Saha, CA Calarge, C Li, Y Liu, JM Fishbaugher, BC Tyler, NM Baker, TL Burns, KF Janz, JC Torner, and SM Levy, "Trabecular bone micro-architecture during SSRI treatment using multi-detector CT imaging and topological analysis on a continuum between plates and rods," Proc. of *Annual Meeting of the American Society for Bone and Mineral Research*, Minneapolis, MN, 2012.

- [32] PK Saha, RE Amelon, Y Liu, C Li, D Jin, C Chen, JM Fishbaugher, EM Letuchy, CA Calarge, KF Janz, DB Hornick, J Eichenberger-Gilmore, TL Burns, JC Torner, and SM Levy, "In vivo study of trabecular and cortical bone in young adults with varying trajectories of bone development using multi-row detector CT imaging," Proc. of *Annual Meeting of the American Society for Bone and Mineral Research*, Baltimore, MD, 2013.
- [33] FW Wehrli, GA Ladinsky, C Jones, M Benito, J Magland, B Vasilic, AM Popescu, B Zemel, AJ Cucchiara, AC Wright, HK Song, PK Saha, H Peachey, and PJ Snyder, "In vivo magnetic resonance detects rapid remodeling changes in the topology of the trabecular bone network after menopause and the protective effect of estradiol," *Journal of Bone and Mineral Research*, **23**, 730-40, 2008, PubMed Central PMCID: PMC2674544.
- [34] XS Liu, AH Huang, XH Zhang, P Sajda, B Ji, and XE Guo, "Dynamic simulation of three dimensional architectural and mechanical alterations in human trabecular bone during menopause," *Bone*, **43**, 292-301, 2008, PubMed Central PMCID: PMC2526101.
- [35] XS Liu, A Cohen, E Shane, E Stein, H Rogers, SL Kokolus, PT Yin, DJ McMahon, JM Lappe, RR Recker, and XE Guo, "Individual trabeculae segmentation (ITS)-based morphological analysis of high-resolution peripheral quantitative computed tomography images detects abnormal trabecular plate and rod microarchitecture in premenopausal women with idiopathic osteoporosis," *Journal of bone and mineral research* **25**, 1496-505, 2010, PubMed Central PMCID: PMC3131618.
- [36] XS Liu, EM Stein, B Zhou, CA Zhang, TL Nickolas, A Cohen, V Thomas, DJ McMahon, F Cosman, J Nieves, E Shane, and XE Guo, "Individual trabecula segmentation (ITS)-based morphological analyses and microfinite element analysis of HR-pQCT images discriminate postmenopausal fragility fractures independent of DXA measurements," *J Bone Miner Res*, **27**, 263-72, 2012, PubMed Central PMCID: PMC3290758.
- [37] PK Saha and BB Chaudhuri, "Detection of 3-D simple points for topology preserving transformations with application to thinning," *IEEE Transaction on Pattern Analysis and Machine Intelligence*, **16**, 1028-1032, 1994.
- [38] PK Saha, Y Xu, H Duan, A Heiner, and G Liang, "Volumetric topological analysis: a novel approach for trabecular bone classification on the continuum between plates and rods," *IEEE Transaction on Medical Imaging*, **29**, 1821-1838, 2010.
- [39] S Majumdar, D Newitt, A Mathur, D Osman, A Gies, E Chiu, J Lotz, J Kinney, and H Genant, "Magnetic resonance imaging of trabecular bone structure in the distal radius: relationship with X-ray tomographic microscopy and biomechanics," *Osteoporos International*, **6**, 376-385, 1996.
- [40] TM Link, S Majumdar, P Augat, JC Lin, D Newitt, Y Lu, NE Lane, and HK Genant, "In vivo high resolution MRI of the calcaneus: differences in trabecular structure in osteoporosis patients," *Journal of Bone and Mineral Research*, **13**, 1175-1182, 1998.
- [41] G Chang, SK Pakin, ME Schweitzer, PK Saha, and RR Regatte, "Adaptations in trabecular bone microarchitecture in Olympic athletes determined by 7T MRI," *Journal of Magnetic Resonance in Medicine* **27**, 1089-1095, 2008, PubMed Central PMCID: PMC3850284.
- [42] S Boutroy, ML Bouxsein, F Munoz, and PD Delmas, "In vivo assessment of trabecular bone microarchitecture by high-resolution peripheral quantitative computed tomography," *The Journal of Clinical Endocrinology and Metabolism*, **90**, 6508-6515, 2005.
- [43] M Burrows, D Liu, and H McKay, "High-resolution peripheral QCT imaging of bone micro-structure in adolescents," *Osteoporosis International*, **21**, 515-520, 2010.
- [44] R Krug, AJ Burghardt, S Majumdar, and TM Link, "High-resolution imaging techniques for the assessment of osteoporosis," *Radiologic Clinics of North America*, **48**, 601-621, 2010, PubMed Central PMCID: PMC2901255.
- [45] SK Boyd, "Site-specific variation of bone micro-architecture in the distal radius and tibia," *Journal of Clinical Densitometry*, **11**, 424-30, 2008.
- [46] R Zhang, J-B Thibault, CA Bouman, KD Sauer, and J Hsieh, "Model-based Iterative Reconstruction for Dual-Energy X-ray CT using a Joint Quadratic Likelihood Model," *IEEE Transactions on Medical Imaging*, **33**, 117-134, 2013.
- [47] JB Thibault, KD Sauer, CA Bouman, and J Hsieh, "A Three-Dimensional Statistical Approach to Improved Image Quality for Multislice Helical CT," *Medical Physics*, **34**, 4526-4544, 2007.
- [48] CA Bouman and K Sauer, "A Unified Approach to Statistical Tomography using Coordinate Descent Optimization," *IEEE Transactions on Image Processing*, **5**, 480-492, 1996.
- [49] W Dong, L Zhang, G Shi, and X Wu, "Image deblurring and super-resolution by adaptive sparse domain selection and adaptive regularization," *IEEE Transactions on Image Processing*, **20**, 1838-1857, 2011.

- [50] C Jiang, Q Zhang, R Fan, and Z Hu, "Super-resolution ct image reconstruction based on dictionary learning and sparse representation," *Scientific Reports*, **8**, 8799, 2018.
- [51] Z Wang, Y Yang, Z Wang, S Chang, J Yang, and TS Huang, "Learning Super-Resolution Jointly from External and Internal Examples," *IEEE Transactions on Image Processing*, **24**, 4359-4371, 2015.
- [52] J Yang, J Wright, TS Huang, and Y Ma, "Image super-resolution via sparse representation," *IEEE Transactions on Image Processing*, **19**, 2861-2873, 2010.
- [53] C Chen, X Zhang, J Guo, D Jin, EM Letuchy, TL Burns, SM Levy, EA Hoffman, and PK Saha, "Quantitative imaging of peripheral trabecular bone microarchitecture using MDCT," *Medical Physics*, **45**, 236-249, 2018.
- [54] AS Chaudhari, Z Fang, F Kogan, J Wood, KJ Stevens, EK Gibbons, JH Lee, GE Gold, and BA Hargreaves, "Super-resolution musculoskeletal MRI using deep learning," *Magnetic Resonance in Medicine*, **80**, 2139-2154, 2018.
- [55] J Park, D Hwang, KY Kim, SK Kang, YK Kim, and JS Lee, "Computed tomography super-resolution using deep convolutional neural network," *Physics in Medicine & Biology*, **63**, 145011, 2018.
- [56] H Yu, D Liu, H Shi, H Yu, Z Wang, X Wang, B Cross, M Bramler, and TS Huang, "Computed tomography super-resolution using convolutional neural networks," Proc. of *2017 IEEE International Conference on Image Processing (ICIP)*, 3944-3948, 2017.
- [57] C You, G Li, Y Zhang, X Zhang, H Shan, S Ju, Z Zhao, Z Zhang, W Cong, MW Vannier, PK Saha, and G Wang, "CT Super-resolution GAN Constrained by the Identical, Residual, and Cycle Learning Ensemble (GAN-CIRCLE)," *IEEE Transactions on Medical Imaging*, **39**, 188-203, 2020.
- [58] Y Chen, F Shi, AG Christodoulou, Y Xie, Z Zhou, and D Li, "Efficient and Accurate MRI Super-Resolution using a Generative Adversarial Network and 3D Multi-level Densely Connected Network," Proc. of *International Conference on Medical Image Computing and Computer-Assisted Intervention*, 91-99, 2018.
- [59] C Ledig, L Theis, F Huszár, J Caballero, A Cunningham, A Acosta, A Aitken, A Tejani, J Totz, and Z Wang, "Photo-realistic single image super-resolution using a generative adversarial network," Proc. of *Proceedings of the IEEE Conference on Computer Vision and Pattern Recognition*, 4681-4690, 2017.
- [60] X Wang, K Yu, S Wu, J Gu, Y Liu, C Dong, Y Qiao, and C Change Loy, "ESRGAN: Enhanced Super-Resolution Generative Adversarial Networks," Proc. of *Proceedings of the European Conference on Computer Vision (ECCV)*, 1-16, 2018.
- [61] JM Wolterink, T Leiner, MA Viergever, and I Išgum, "Generative Adversarial Networks for Noise Reduction in Low-Dose CT," *IEEE Transactions on Medical Imaging*, **36**, 2536-2545, 2017.
- [62] I Goodfellow, J Pouget-Abadie, M Mirza, B Xu, D Warde-Farley, S Ozair, A Courville, and Y Bengio, "Generative adversarial nets," Proc. of *Advances in Neural Information Processing Systems*, 2672-2680, 2014.
- [63] EH Meijering, WJ Niessen, JP Pluim, and MA Viergever, "Quantitative comparison of sinc-approximating kernels for medical image interpolation," Proc. of *International Conference on Medical Image Computing and Computer-Assisted Intervention*, 210-217, 1999.
- [64] PA Yushkevich, J Piven, HC Hazlett, RG Smith, S Ho, JC Gee, and G Gerig, "User-guided 3D active contour segmentation of anatomical structures: significantly improved efficiency and reliability," *Neuroimage*, **31**, 1116-1128, 2006.
- [65] K He, X Zhang, S Ren, and J Sun, "Delving deep into rectifiers: Surpassing human-level performance on imagenet classification," Proc. of *Proceedings of the IEEE International Conference on Computer Vision*, 1026-1034, 2015.
- [66] DP Kingma and J Ba, "Adam: A method for stochastic optimization," *arXiv preprint arXiv:1412.6980*, 2014.
- [67] ML Bouxsein, SK Boyd, BA Christiansen, RE Guldborg, KJ Jepsen, and R Muller, "Guidelines for assessment of bone microstructure in rodents using micro-computed tomography," *Journal of Bone and Mineral Research*, **25**, 1468-1486, 2010.
- [68] Y Liu, D Jin, C Li, KF Janz, TL Burns, JC Torner, SM Levy, and PK Saha, "A robust algorithm for thickness computation at low resolution and its application to in vivo trabecular bone CT imaging," *IEEE Transactions on Biomedical Engineering*, **61**, 2057-2069, 2014, PubMed Central PMCID: PMCNIHMSID696943.
- [69] PK Saha, D Jin, Y Liu, GE Christensen, and C Chen, "Fuzzy object skeletonization: theory, algorithms, and applications," *IEEE Transactions on Visualization and Computer Graphics*, **24**, 2298-2314, 2018.
- [70] Z Wang, AC Bovik, HR Sheikh, and EP Simoncelli, "Image quality assessment: from error visibility to structural similarity," *IEEE Transactions on Image Processing*, **13**, 600-612, 2004.